



Cite this: *Nanoscale*, 2025, **17**, 14394

## Photocurable cellulose nanofibers and their copolymers with polyacrylamide as microgels to support 3D cell cultivation†

Shujun Liang,<sup>a,b</sup> Qingbo Wang,<sup>b</sup> Chunlin Xu,<sup>b</sup> <sup>b</sup> Jessica M. Rosenholm <sup>a</sup> and Xiaoju Wang \*<sup>a,b</sup>

Cellulose nanofibers (CNFs) are renewable bionanomaterials with great utilization potential in future biomedical. However, conventional CNF hydrogels are limited by low structural flexibility and insufficiently tunable mechanical properties, restricting their use in 3D cell culture systems. To address these limitations, we developed granular hydrogel platforms using photocurable and ionically crosslinkable methacrylated CNFs (CNFMAs) and their copolymers with polyacrylamide *via* a dual cross-linking mechanism. By employing this bottom-up approach, mechanically fragmented microgels were reassembled into granular hydrogels *via* calcium ion crosslinking. This assembly of methacrylated CNF-based microgels successfully supported long-term 3D cell culture and demonstrated the capability to provide biomechanical cues that facilitate different cellular responses. The granular hydrogel of CNFMA alone promoted clustering and migration of human pancreatic cancer cells (PANC-1), while the copolymerization of CNFMA with polyacrylamide introduced stiffness variations into the hybrid granular hydrogel system that enhanced the spreading of preosteoblasts (MC3T3-E1) and facilitated spheroid formation in the culture of PANC-1. These findings underscore the versatility of photocurable nanocellulose in constructing biomaterial platforms. Overall, this study establishes a foundation for advancing *in vitro* models for tissue engineering and cancer research using CNFMA-derived microgel systems.

Received 9th February 2025

Accepted 9th May 2025

DOI: 10.1039/d5nr00583c

rsc.li/nanoscale

## 1. Introduction

“Life in 3D is never flat”.<sup>1</sup> Three-dimensional (3D) cell culture models have become increasingly prevalent in *in vitro* laboratory studies across various domains of life science, such as cancer biology, stem cell research, and disease modeling.<sup>1–3</sup> 3D cell models provide a more physiologically relevant environment compared with conventional two-dimensional (2D) cultures. In 2D cultures on tissue culture plastics, the absence of biorelevant mechanics and nutrient gradients leads to unnatural cell morphology and limited functionality. The spatiotemporally restricted cell–cell and cell–matrix interactions may impair proper differentiation and behavior.<sup>2,4,5</sup> For instance, osteoblasts become flattened, and tumor cells grow in simple monolayers, failing to mimic the complex cellu-

lar behavior and response in *in vivo* conditions.<sup>2,6,7</sup> In contrast, 3D cell models (*e.g.*, cell spheroids, organoids, and hydrogel-based 3D cell culture scaffolds) better replicate the architecture, mechanical characteristics, gradients of nutrients, and metabolism products in native tissues. Over the past decade, significant advancement has propelled the development of biomaterial hydrogel scaffolds, which are delicately engineered to mimic and replicate microenvironmental aspects of a natural extracellular matrix (ECM).<sup>8–10</sup> These hydrophilic and interpenetrating networks of hydrogel scaffolds are constructed using synthetic polymers, natural polymers, or their hybrids through physicochemical interactions or covalent bonding.<sup>9,11</sup> In this context, poly(ethylene glycol) (PEG)- and polyacrylamide (PAA)-based synthetic polymers have been significantly considered owing to their great biocompatibility and macromolecular attributes of high molecular weight and tunable chemistry, which facilitate precise regulation of the mechanical properties and degradation rates of hydrogels.<sup>12,13</sup> However, their bio-inertness or lack of biological moieties often requires affinity manipulation through surface conjugation of adhesion factors, such as RGD peptides, enabling adhesion of cells to the matrix.<sup>11,14</sup> Natural polymers derived from animal, marine, and plant sources, such as collagen,

<sup>a</sup>Pharmaceutical Sciences Laboratory, Faculty of Science and Engineering, Åbo Akademi University, Biocity (3rd floor), Tykistökatu 6A, Turku FI-20520, Finland. E-mail: xwang@abo.fi

<sup>b</sup>Laboratory of Natural Materials Technology, Faculty of Science and Engineering, Åbo Akademi University, Henrikinkatu 2, Turku FI-20500, Finland

† Electronic supplementary information (ESI) available. See DOI: <https://doi.org/10.1039/d5nr00583c>



chitosan, and alginate, have been widely exploited in fabrication of 3D hydrogel-scaffold models owing to their inherent biocompatibility and closer resemblance to native ECM. Nonetheless, natural protein hydrogels derived from animal sources, such as collagen and Matrigel, have also been the subjects of controversy owing to their potential immunogenicity, batch-to-batch variability and ethical concerns associated with animal-derived components.<sup>15</sup>

Xeno-free hydrogel biomaterials are alternatively sought after to ensure consistent quality and to reduce the immunogenic risk in such applications as 3D cell culture and therapeutic scaffolds.<sup>16,17</sup> Applying sustainable biomaterials derived from renewable plant sources is a growing trend in pharmaceutical and biomedical applications. In this context, cellulose nanofibers (CNFs) physically present in a hydrogel form of entangled one-dimensional nanofibers at very low concentrations (<1 wt%) are proven to be successful nanomaterials as 3D cell culture scaffolds.<sup>18–20</sup> This is mainly attributed to their high water-retention capacity and fibrous nano-topography, which mimics the native ECM to a large extent and exhibits excellent biocompatibility. The synthesis of CNFs predominantly involves tuning surface chemistry,<sup>21</sup> specifically functionalizing its abundant surface hydroxyl groups. Various functional derivatives have been tailored for biomedical applications.<sup>22,23</sup> For instance, amino-functionalized cellulose nanofibers enable the active sites to undergo further conjugation with bioresponsive molecules, facilitating antimicrobial properties,<sup>24</sup> while phosphorylated CNF stimulates early osteogenic differentiation of preosteoblasts and promotes the macroscopic biomineralization within a composite hydrogel.<sup>25</sup> Anionic CNFs, with their introduced carboxyl groups ( $-\text{COO}^-$ ) via TEMPO-oxidation, exhibit superior dispersibility and uniformity, offering reactive sites for further chemical or physical crosslinking. TEMPO-CNF hydrogels have demonstrated excellent biocompatibility in hydrogel 3D cell cultures.<sup>26–28</sup> Notably, CNFs with this specialized surface chemistry, such as the commercially available anionic GrowDex®, have been validated for cultivating a wide range of cell types.<sup>29,30</sup>

Despite the exciting advancements of CNF hydrogels in biomedical fields, these nanomaterial-based hydrogels still face several development challenges to effectively support 3D cell culture, *e.g.*, providing the biophysical and biochemical cues within the biomaterial system to guide cellular responses.<sup>31</sup> Nanofibers in CNF hydrogels offer appealing nano-fibrillar topography rendering cell adhesion and an extremely large surface area to interface with the accommodated living cells. Meanwhile, the entanglement of nanofibers only results in nano-scale porosity. In 3D cell culture, the cell migration and infiltration throughout the hydrogel matrix necessitates the presence of macropores in the hydrogel structure. Meanwhile, local mechanical properties such as matrix stiffness and elasticity of the hydrogel are core biophysical cues to direct cell responses (adhesion, migration and differentiation) through cellular mechanosensing to the surrounding microenvironments. To optimize the biomechanical cues, the mechanical properties in hydrogels have been emphasized for their role in

regulating cell behaviors and enhancing tissue regeneration.<sup>32,33</sup> Correspondingly, the hydrogel material design in the 3D cell culture model shall offer tunable control over the matrix mechanics. For the pristine CNF hydrogel,<sup>32</sup> this commonly relies on adjustment to the CNF concentration (solid content), which is poor in capacity of defining the local matrix stiffness and yields only nano-scale porosity.<sup>34,35</sup> Other approaches have been devised to address the above perspectives, such as the incorporation of biocompatible porogens/additive or the assembly of enzyme-incorporated microgels. These processes are generally labor-intensive and often cannot guarantee the complete elimination of impurities.<sup>36–38</sup> The jamming of granular microgels is a constructive method for creating macroporosity within a monolithic hydrogel. As a bottom-up strategy, it has been applied with successful outcomes in various biomaterial systems for 3D cell culture and biofabrication.<sup>39–41</sup> For instance, Gehlen *et al.* have developed a method using calcium ion crosslinking to reassemble fragmented TEMPO-oxidized CNF microgels into irregularly stacked, porous granular hydrogels.<sup>42</sup> These structures maintain mechanical integrity while significantly enhancing the uniform 3D distribution and migration of fibroblasts and promoting effective cellular integration and function within the scaffold.

As one of the latest advancements in the field of nanocellulose for biomedical, our previous study reported the synthesis of photocurable CNF with surface modification of methacryloyl ( $-\text{MA}$ ) groups, following the TEMPO-oxidation to impart anionic carboxyl groups.<sup>43</sup> This nanomaterial of methacrylated TEMPO-oxidized CNF (CNFMA) manifests dual functions: it is photocurable *via* free-radical chain polymerization and physically crosslinkable by  $\text{Ca}^{2+}$  with the abundant carboxyl groups. When CNFMA is subjected to copolymerization with acrylamide under UV-irradiation, it forms a strong and more elastic hydrogel network of nanofibers that are covalently bridged by short and linear chains of polyacrylamide (PAA).<sup>43</sup> This hybrid hydrogel is highly transparent and has an appealing shape-memory material characteristic. As a hydrogel matrix for 2D cell culture, it greatly supports the cell adhesion and proliferation of fibroblasts and HeLa cancer cells. More importantly, this reaction route supports a tunable control over the mechanical properties of the hydrogel in a wide range of compression modulus of 5–15 kPa, by facilely adjusting the concentrations of CNFMA and acrylamide monomers.

To develop more effective and versatile CNF-based 3D cell culture platforms; herein, we propose to adopt the bottom-up strategy of granular microgel with photocurable CNFMA alone or hybrid CNFMA + PAA (CMPAA) hydrogels. The microgel fabrication and their assembly in 3D cell culture have leveraged the dual crosslinking mechanism associated with photocurable and anionic CNFMA through UV-induced photocuring and ionic cross-linking. We deployed mechanical fragmentation to the photocured bulk hydrogels by passing them through mesh filters of varying sizes (150  $\mu\text{m}$  and 60  $\mu\text{m}$ ) to control the dimension of the resulting microgels as well as the porosity fraction in assembled granular hydrogels. Unlike



conventional CNF hydrogels that solely rely on physical jamming or unimodal crosslinking, the dual-crosslinkable CNFMA system allows efficient production of nanocellulose microgels that retain structural integrity during calcium-mediated assembly into interconnected, porous granular hydrogels. Notably, the presence of methacrylate groups allows versatile matrix polymer functionalization either through copolymerization with other photocurable monomers, such as the acrylamide in our current study, or through photocrosslinking with other macromers, such as polyethylene glycol diacrylate (PEGDA) or gelatin methacrylate (GelMA). In this study, the hybrid of polyacrylamide further broadened the mechanical tunability of the system and facilitated modulation of matrix stiffness through copolymerization with CNFMA, thereby enhancing its adaptability to support diverse cellular behaviors. These tailored hydrogel platforms created an optimized microenvironment, supporting the growth and viability of MC3T3-E1 preosteoblasts and PANC-1 human pancreatic cancer cells in 3D culture for up to 14 days. Notably, the mechanical cues provided by CNFMA alone system and hybrid CMPAA systems have elicited distinct cellular responses towards different cell types. Our study aims to provide new and practical approaches for utilizing renewable nanomaterial CNF to support 3D cell cultures. This includes an integrated workflow for cell handling within a laminar hood and enhanced tunability of hydrogel matrix to meet cell type-specific biochemical and biophysical requirements.

## 2. Experimental section

### 2.1 Materials

CNFMA was synthesized as previously described by dispersing TEMPO-oxidized cellulose fibers (7.8 wt%, 1.25 mmol g<sup>-1</sup> charge) in DMF, followed by activation with triethylamine and modification with methacrylic anhydride. The reaction was stirred overnight, and the fibers were thoroughly washed with water and concentrated to approximately 10 wt%. The resulting dispersion was stored under cold, dark conditions. Before use, the dispersion was homogenized to ensure consistency.<sup>43</sup> All chemicals were purchased from Sigma-Aldrich unless otherwise specified.

### 2.2 Formulation of hydrogels and microgel fabrication

CNFMA (1.2 wt%) was diluted in a buffer solution to prepare both CNFMA-only hydrogels and CNFMA-polyacrylamide (CMPAA) copolymer hydrogels. The final concentrations were 0.6 wt% CNFMA or 0.75 wt% CNFMA for the pure CNFMA system and 0.6 wt% CNFMA + 0.6 wt% PAA or 0.75 wt% CNFMA + 0.75 wt% PAA for the CMPAA system. The buffer solution was prepared using 20 mM HEPES and 823 mM mannitol, and the final mannitol concentration adjusted to 160 mM. For both hydrogel systems, 2 w/v% lithium phenyl-2,4,6-trimethylbenzoylphosphinate (LAP, 98%, TCI) dissolved in 20 mM HEPES buffer was used as the photoinitiator.

The obtained 0.6/0.75CNFMA and 0.6/0.75CMPAA were mixed well and the air bubbles were removed by vortexing and ultrasonication. CNFMA-only and CMPAA copolymer hydrogels were primarily photo-crosslinked into bulk hydrogels with a large-format curing light source for 10 minutes (405 nm, EFL-LS1602, Yongqinquan Intelligent Equipment). 0.6/0.75CMPAA bulk hydrogels were first washed with Milli-Q water for 5 minutes to remove the potential acrylamide residual monomer and free PAA. Both bulk hydrogels were further passed through the syringe holder equipped with either a 150 μm or 60 μm support screen (ADVANTEC MFS, Inc.) The resulting microgels were labeled as 0.6CNFMA/150, 0.6CNFMA/60, 0.75CNFMA/150, 0.6CNFMA/60, 0.6CMPAA/150, 0.6CMPAA/60, 0.75CMPAA/150, and 0.75CMPAA/60.

### 2.3 Grafted PAA analysis

A mass balance approach was employed to quantify the grafted PAA in the 0.6CMPAA and 0.75CMPAA systems. Hydrogels were prepared following the procedure outlined in Section 2.2 while using Milli-Q water for all solution preparations. After photocrosslinking, the bulk hydrogels were washed with Milli-Q water for 5 minutes, and the washing solution was collected for analysis. Both the washed hydrogels and the collected washing solution were subsequently freeze-dried. The grafted PAA content was determined by comparing the weights of the hydrogels before and after freeze-drying.

### 2.4 Rheological and mechanical properties analysis

The rheological properties of the samples were measured using an Anton Paar Physica MCR 702 rheometer (Anton Parr GmbH) with a parallel plate geometry using a 25 mm diameter plate and a 0.5 mm gap distance at 25 °C. Viscosity curves were recorded *via* shear flow measurements, with the shear rate ramping from 0.01 to 1000 s<sup>-1</sup>. The photo-crosslinking kinetics of the hydrogels were evaluated in oscillation mode, with a gap distance of 20 μm, at a constant oscillatory strain of 1% and a frequency of 1 Hz. Irradiation was initiated 30 seconds into the experiment using a 405 nm light source (20 mW cm<sup>-2</sup>, bluepoint LED eco, Hönle Group) through a transparent glass bottom plate, and the storage modulus (*G'*) was recorded. The samples were pre-sheared at 100 s<sup>-1</sup> for 30 seconds and allowed to rest for 60 seconds to reach equilibrium before each test. Amplitude sweep measurements were conducted over a strain range of 0.01% to 500% at a constant frequency of 1 Hz, with data acquisition set at 10 seconds per data point and the temperature maintained at 25 °C.

The indentation experiments of the granular hydrogel were conducted using a Piuma nanoindenter (Optics 11 Life, Amsterdam). A cantilever-based probe equipped with a spherical tip of 50 μm was utilized, with a cantilever stiffness of 0.44 N m<sup>-1</sup> and a calibrated Geo factor of 2.62. The measurements were performed in controlled load indentation mode, and Young's modulus were recorded. For each sample, at least 20 points were selected for measurement. All experiments were carried out at room temperature in PBS buffer.



## 2.5 Microgels staining

Microgels were stained by preparing a 10% (v/v) solution by diluting 100  $\mu\text{L}$  of CNFMA microgels in 1 mL of 20 mM HEPES buffer. After dilution, 25  $\mu\text{L}$  of calcofluor white was added, and the mixture was incubated in a 37  $^{\circ}\text{C}$  water bath for 30 minutes. Then, confocal images were captured using a 3i Marianas CSU-W1 spinning disk confocal microscope under 488 nm excitation (50  $\mu\text{m}$  pinholes, Intelligent Imaging Innovations GmbH).

## 2.6 Porosity analysis

The granular hydrogels were stained with calcofluor white at a concentration of 3% (v/v) in PBS buffer and incubated at 37  $^{\circ}\text{C}$  for 60 minutes. Confocal images were acquired using a 3i Marianas CSU-W1 spinning disk confocal microscope under 488 nm excitation (50  $\mu\text{m}$  pinholes, Intelligent Imaging Innovations GmbH). A depth of 100  $\mu\text{m}$  was imaged, with a 1  $\mu\text{m}$  gap between adjacent optical sections. The fluorescent area in each stack was excluded using the open-source software Image J and averaged across the entire stack. The obtained stacks were reconstructed with Imaris 10.2.

## 2.7 3D cell culture evaluation with the granular hydrogels

All cell culture reagents were obtained from Gibco unless otherwise specified. The MC3T3-E1 cell line derived from mouse (99072810) and the human PANC-1 cancer cell line (CRL-1469<sup>TM</sup>) were purchased from Sigma-Aldrich and ATCC, respectively. MC3T3-E1 cells were cultured in a complete medium composed of minimum essential medium (MEM $\alpha$ ) supplemented with 10% fetal bovine serum (FBS), 2 mM glutamate, and 100 U mL<sup>-1</sup> penicillin-streptomycin (Pen-strep). MC3T3-E1 cells were passaged approximately once a week, and the culture medium was changed every other day. Similarly, PANC-1 cells were maintained in a complete medium consisting of Dulbecco's modified Eagle's medium (DMEM) supplemented with 10% FBS and 100 U mL<sup>-1</sup> Pen-strep, with the medium also changed every other day. All cells were incubated in a humidified environment with 5% CO<sub>2</sub> at a constant temperature of 37  $^{\circ}\text{C}$ . PANC-1 cells were passaged approximately twice a week. Only MC3T3-E1 cells and PANC-1 cells before passage 15 were utilized in this study.

The microgels (0.6CNFMA/150, 0.75CNFMA/150, 0.6CMPAA/150, and 0.75CMPAA/150) were diluted to 80% with their respective cell culture medium and allowed to equilibrate overnight. MC3T3-E1 and PANC-1 cells from the same passage were harvested and gently resuspended in the microgels at a density of 1.5 million cells per mL using gentle pipetting. A 65  $\mu\text{L}$  aliquot of the cell-laden microgels was loaded into a non-cell culture-treated 96-well plate (Nunc MicroWell 96-well microplates, Thermo Scientific) to eliminate interference from metabolic activity signals of any cells adhering to the plate surface. 100 mM of sterilized CaCl<sub>2</sub> was used for secondary crosslinking for 1 min. Then, the granular hydrogels were washed with PBS for 10 minutes, and repeated 3 times to remove the residual CaCl<sub>2</sub> and PAA. Then, the cell-laden granu-

lar hydrogels were cultured for 14 days in an incubator with 5% CO<sub>2</sub> at a constant temperature of 37  $^{\circ}\text{C}$ .

The proliferation and viability of MC3T3-E1 and PANC-1 cells at certain time points (day 1, day 7, and day 14) were evaluated by a cell counting kit-8 (CCK-8) assay and live/dead assay, respectively. Briefly, the CCK-8 testing reagent was prepared by diluting the CCK-8 agent (CK04-11, Dojindo) tenfold with the corresponding cell culture medium. The cell culture medium in each well was replaced with 150  $\mu\text{L}$  of CCK-8 testing reagent-containing medium, and the cell-laden granular hydrogels were incubated for 4 hours in the incubator. Following incubation, 100  $\mu\text{L}$  of the medium was transferred to a separate 96-well plate for absorbance measurement at 450 nm using a spectral scanning multimode reader (Varioskan Flash, Thermo Scientific). Live/dead cell staining kit II (PromoKine) was used for the live/dead assay. Briefly, the cell-laden granular hydrogels were immersed in 200  $\mu\text{L}$  of the staining solution (0.5  $\mu\text{M}$  Calcein-AM and 1.6  $\mu\text{M}$  EthD-III, diluted in PBS) for 3 hours in an incubator after being washed with PBS. Fluorescence microscopy images were captured using a 3i Marianas CSU-W1 spinning disk confocal microscope (50  $\mu\text{m}$  pinholes, Intelligent Imaging Innovations GmbH), with 1  $\mu\text{m}$  spacing between optical sections.

Cytoskeleton staining was performed to assess the spreading and morphology of MC3T3-E1 and PANC-1 cells within the granular hydrogels. At specific time points (day 1, day 7, and day 14), cell-laden granular hydrogels were fixed with 4% paraformaldehyde for 10 minutes at room temperature, followed by permeabilization with a 0.1% Triton X-100 solution for 5 minutes at 4  $^{\circ}\text{C}$ . The hydrogels were then incubated in a 1% bovine serum albumin solution at 37  $^{\circ}\text{C}$  for 30 minutes. Subsequently, F-actin was stained using Alexa 488-phalloidin dye (330 nM, Cell Signaling Technology) for 1 hour, and nuclei were stained with DAPI (300 nM, Cayman Chemical) for 10 minutes. After staining, the cell-laden hydrogels were washed with PBS and stored at 4  $^{\circ}\text{C}$  in the dark. Fluorescence microscopy images of the stained cells were acquired using a 3i Marianas CSU-W1 spinning disk confocal microscope (50  $\mu\text{m}$  pinholes, Intelligent Imaging Innovations GmbH), with imaging conducted at 1  $\mu\text{m}$  spacing between optical sections. All the obtained stacks were reconstructed with Imaris 10.2 for 3D visualization.

**Statistical analysis.** all data were analyzed using one-way or two-way analysis of variance (ANOVA) in GraphPad Prism 9. Statistical significance was indicated as  $p < 0.05$ ,  $p < 0.01$ ,  $*p < 0.001$ , and  $**p < 0.0001$ . Each experiment was performed at least three times, and the results are presented as the mean  $\pm$  SD.

## 3. Results and discussion

### 3.1 Microgel and granular hydrogel fabrication

The 1D nanomaterials in the CNF hydrogel offer a fibrous network that closely mimics the ECM. However, native CNF lacks the functional groups needed to create crosslinking net-



works essential for maintaining the mechanical integrity of the hydrogel during long-term culture. TEMPO oxidation is a common method to enhance the colloidal dispersity of CNFs by introducing carboxyl groups. This pretreatment to cellulose pulp selectively induces oxidation of hydroxyl groups at the C6 position in cellulose, which is then followed by mechanical defibrillation to produce nanofibers with diameters of 5–60 nm and lengths up to several micrometers.<sup>44</sup> The introduction of abundant carboxyl groups enhances hydrophilicity and enables the formation of ionic crosslinked networks, significantly improving its adaptability for cell culture.<sup>44</sup> With our synthesis methods, CNFMA synthesized with TEMPO oxidation under neutral conditions demonstrates an anionic charge content of  $0.66 \pm 0.06 \text{ mmol g}^{-1}$  and a degree substitution (DS) of methacryloyl of  $4.3\% \pm 0.05\%$  remained after autoclave sterilization. During the high-pressure and temperature sterilization, partial degradation of carboxyl groups and methacryloyl groups is inevitable.<sup>45</sup> However, this trade-off is necessary to ensure the sterility of CNFMA for biomedical applications. Despite this, the remaining charge content is sufficient to maintain dispersibility of entangled nanofibers, rendering suitable viscoelastic properties to present as a stable hydrogel even at a low selected concentration of 0.6 wt%. According to what was earlier studied by Metwally *et al.* and Liu *et al.*, this intermediate level of anionic charge on nanofiber surface is proper for cell–matrix reactions.<sup>46,47</sup> The remained DS of methacryloyl on nanofiber also supports fast photo-crosslinking with arylamide monomer, enabling the fabrication of hydrogels with tailored network properties. Sterilizing the CNFMA hydrogel *via* an autoclave makes it feasible to use these biomaterials in standard cell culture laboratory settings. To further elucidate the differences between the CNFMA and traditional TEMPO-CNF system, Table 1 presents a detailed comparison focusing on mechanical properties, structural flexibility, and advantages for 3D cell culture.

As illustrated in Scheme 1, the fabrication process of the granular hydrogel involves three key steps. First, the bulk hydrogel is photocured to either crosslink the methacryloyl groups on CNFMA or copolymerize CNFMA with acrylamide monomers (AAMs) *via* photo-induced free-radical chain polymerization. The precise nature of the hydrogel network depends on whether the system comprises only covalently crosslinked nanofibers or a hybrid copolymer matrix of CNFMA-PAA. For the 0.6CMPAA and 0.75CMPAA systems, the grafted PAA content was determined as approximately 87% of monomer used in the hydrogel preparation. During the photopolymerization, the remaining monomer has been converted as the homopolymer of PAA that is not covalently bridged with nanofibers and remains water soluble in the washing step. Both systems showed excellent stability in water after photocrosslinking (Fig. S1†). Second, high shear forces are applied to the bulk hydrogel in the mechanical fragmentation to force the bulk hydrogel to pass through sieves of varying mesh sizes. The combined mechanical stress and constraint of the sieve cause the interconnected fibers to fragment, resulting in the formation of discrete microgels. This process not only disrupts

**Table 1** Comparison of the CNFMA system and traditional TEMPO-CNF hydrogel for 3D cell culture

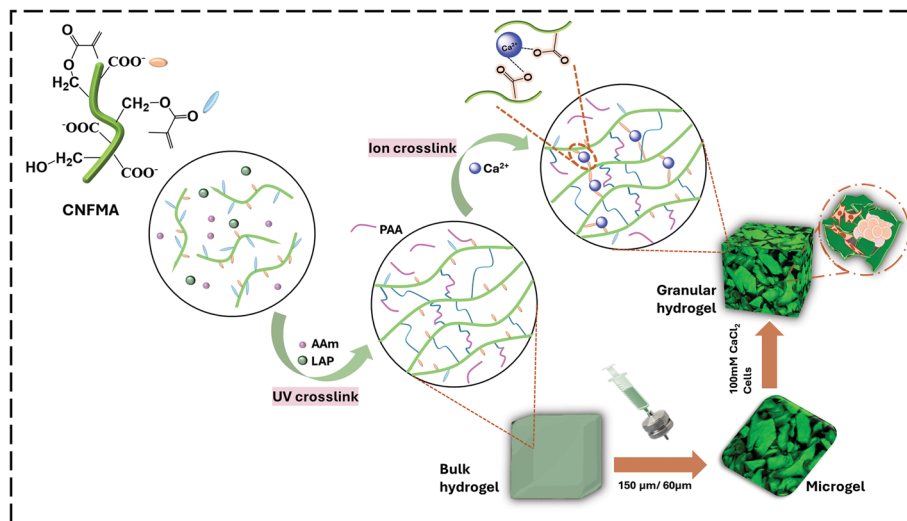
Parameter	Dual-crosslinkable CNFMA hydrogel	Traditional TEMPO-CNF hydrogel
Gelation method	Dual crosslinking <i>via</i> photopolymerization and ionic bonding, enabling tunable and rapid gelation	Primarily ionic crosslinking; gelation limited by ionic strength and nanofibril packing
Structural flexibility	High compositional and structural flexibility through photopolymerization with other monomers and macromers	Limited flexibility due to rigid fibrillar network and strong hydrogen bonding
Mechanical properties	Broad range of stiffness <i>via</i> controllable crosslinking density and polymer ratio	Moderate tunability; stiffness largely dependent on entangled nanofibril concentration and ionic interactions
Biocompatibility and bioactivity	Supports enhanced cell spreading, proliferation, and bioactivity through tailored chemistry and network porosity	Suitable for basic cell encapsulation; lacks customized bioactive features

covalent bonds in localized areas but also exposes functional groups such as carboxylate groups on the surface of the fragmented microgels. Lastly, these exposed carboxylate groups subsequently form coordination bonds with  $\text{Ca}^{2+}$  (at a concentration of 100 mM), enabling the reassembly of fragmented microgels into granular hydrogels. The resulting granular hydrogel is characterized by a randomly packed structure with open and interconnected pores. This architecture facilitates nutrient diffusion and cell migration, making it suitable for supporting the cultivation of MC3T3-E1 pre-osteoblasts and PANC-1 cancer cells.

### 3.2 Rheological and mechanical properties

Rheological properties are crucial in hydrogel fabrication, as rheological characterization ensures that the hydrogel has the proper consistency to provide a stable and supportive matrix for cell encapsulation and growth. Understanding rheological behavior allows for the optimization of gelation conditions, network formation, and mechanical strength of the fabricated hydrogel.<sup>48–50</sup> The viscosities of the hydrogels after photocrosslinking and the resulting microgels were measured using ramp-up and ramp-down shear rate experiments. As shown in Fig. 1A–D, all the hydrogels and microgels exhibit typical shear-thinning behavior, as the nanocellulose and its copolymer PAA chains align in the direction of shear, reducing resistance to flow. The shear-thinning behavior is beneficial for the pipetting during the granular hydrogel preparation processing. With increasing CNFMA and PAA content, the viscosity gradually increases. Hysteresis-like behavior was inferred from the viscosity profiles of all hydrogel samples, even though the measurements were performed in zwitterionic HEPES buffer.





**Scheme 1** Illustration of the fabrication process of granular hydrogels via photo-crosslinking and ionic-crosslinking.

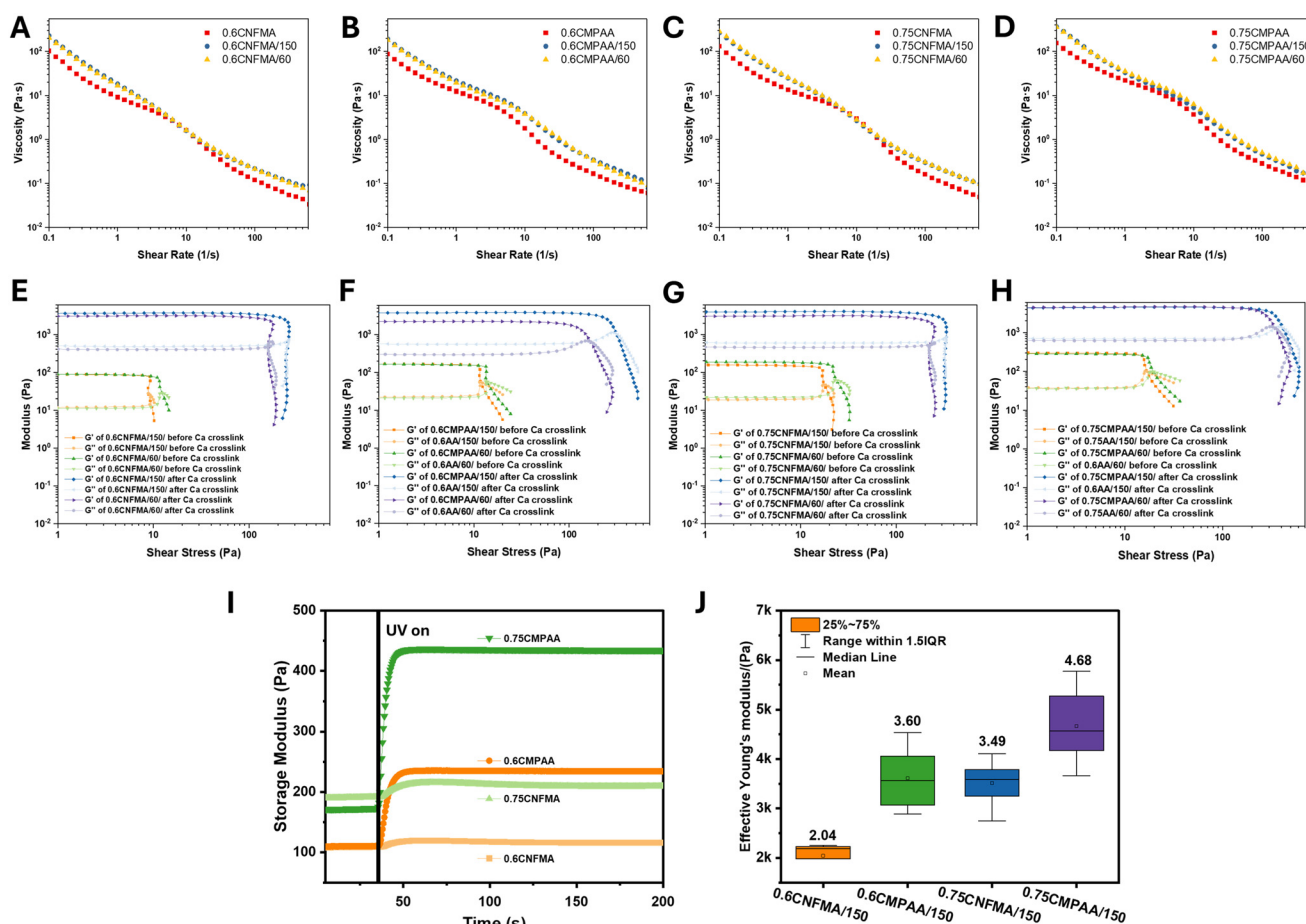


**Fig. 1** Rheological and mechanical properties of the formulated systems. (A–D) Viscosity curves of the formulated hydrogels as a function of shear rate. (E–H) Amplitude sweep comparison of formulated microgels before and after  $\text{Ca}^{2+}$  crosslinking plotted against shear stress. (I) Photo-responsive behavior of the hydrogels under a 405 nm ( $20 \text{ mW cm}^{-2}$ ) light source. (J) Effective Young's modulus of the granular hydrogels measured via nanoindentation.



The buffer was selected to maintain physiological pH while minimizing electrostatic screening effects. Despite this, the observed viscosity response suggests structural rearrangements typical of CNF-based systems. This behavior is likely attributed to the inherent tendency of cellulose nanofibrils to form flocs, which partially dissociate under increasing shear rates but do not immediately re-form upon shear cessation or reduction. Such delayed recovery of the fibrillar network can result in time-dependent viscosity changes, consistent with hysteresis reported in similar systems.<sup>25,50</sup> Additionally, when the hydrogels were fragmented into microgels of varying sizes, an increase in viscosity was observed. This effect may be related to altered network reformation dynamics in the microgel suspensions, where the higher surface area-to-volume ratio and increased effective volume fraction promote stronger interparticle interactions and tighter packing during rest.

The dominant rheological behavior of microgels and the effects of polymer concentration, particle size, and  $\text{Ca}^{2+}$  crosslinking on flow transition were characterized by the amplitude sweep against shear stress; the amplitude sweep can be further used to determine the linear viscoelastic region (LVER). As shown in Fig. 1E–H, storage modulus ( $G'$ ) consistently exceeded loss modulus ( $G''$ ) across all samples, indicating a typical predominant elastic behavior of the CNF-based hydrogel.

In samples with photo-crosslinking and subsequent  $\text{Ca}^{2+}$  crosslinking, the size of microgels and the crosslinking method significantly influenced either flow stress ( $\tau_f$ ) or structural stability. Before  $\text{Ca}^{2+}$  crosslinking, the size of the microgels has a relatively minor effect on the modulus, indicating that the covalent bonds formed through photopolymerization primarily provide basic elasticity and a stable network structure. However, microgels processed through a 60  $\mu\text{m}$  mesh exhibited increased specific surface area due to particle fragmentation, resulting in higher flow  $\tau_f$ . This behavior may be attributed to a more compact structure and stronger interparticle interactions, which can slow the flow transition. After  $\text{Ca}^{2+}$  crosslinking, samples that were processed through a 150  $\mu\text{m}$  mesh exhibited higher  $\tau_f$ , potentially due to the larger particle rigidity and the dynamic crosslinking compensating for deficiencies of the primary network structure. Furthermore, the addition of  $\text{Ca}^{2+}$  dramatically increased the yield stress ( $\tau_y$ ), indicating enhanced network stiffness and mechanical integrity. This enhancement is attributed to dynamic crosslinking points formed by  $\text{Ca}^{2+}$  interacting with  $-\text{COO}^-$  through electrostatic and coordination interactions. These crosslinking points fill the loose regions within the photopolymerized network, thereby improving its integrity and density, as evidenced by the significant increase in the resistance to flow.

Notably, the 0.6/0.75CNFMA samples displayed a lower flow transition index ( $\tau_f/\tau_y$ ) compared with the 0.6/0.75CMPAA samples. Specifically, a sudden drop of  $G'$  was observed after  $\text{Ca}^{2+}$  crosslinking in the 0.6/0.75CNFMA samples. This observation indicates that the incorporation of PAA facilitates the transition of the material from brittle to soft.<sup>51</sup> 0.75CMPAA samples exhibited the highest modulus and the largest  $\tau_y$ , with

the influence of microgel size on the modulus and resistance to flow significantly reduced. It is suggested that a dense polymer network can minimize the effect of particle size, resulting in consistent rheological properties across different mesh sizes.

Fig. 1I–J illustrate the dynamic modulation of the mechanical properties of hydrogels through a dual-crosslinking mechanism. To monitor the photoreaction kinetics of the hydrogel under UV irradiation, photorheology was applied to record the changes in  $G'$  over time in real-time under constant strain of 1% and a frequency of  $1 \text{ s}^{-1}$ . Before UV exposure, the storage modulus of the hydrogel precursor ( $G' < 200 \text{ Pa}$ ) was relatively low, exhibiting fluid-like characteristics and indicating the absence of an effectively crosslinked network. Upon UV irradiation,  $G'$  increased rapidly, reaching a stable plateau within less than 20 seconds. This rapid increase suggested a highly efficient formation of a primary crosslinking network based on photocrosslinking or photopolymerization of methacryloyls in a short time. Furthermore, the co-polymerization between methacryloyls and acrylamide significantly contributed to the enhancement of the plateau modulus, especially for the 0.75CMPAA hydrogel (Fig. 1I).

The effective Young's modulus of granular hydrogels was determined using a nanoindentation instrument since the nanoindentation technology supports assessments on local elastic properties at the microscale, which closely approximates the perception of material stiffness by microenvironmental entities such as cells.<sup>52</sup> The results showed that  $-\text{COO}^-$  exposed on the CNF surface formed an effective secondary crosslinking network with calcium ions within 1 minute, even at a concentration of 100 mM (Fig. 1J). Following secondary crosslinking, the effective (reduced) Young's moduli of the granular hydrogels ranged within 2.04–4.68 kPa, suggesting a tunable elastic property. Additionally, a comparison of the effective Young's modulus distributions of CMPAA and CMFMA hydrogels revealed that CMPAA exhibited greater variability within a 1.5 $\times$  interquartile range (IQR). This variability indicates an uneven distribution of PAA within the hydrogel, leading to localized stiffness gradients. Such finely tuned gradient stiffness is considered advantageous to better mimic the complex mechanical conditions while providing the mechanical cues for the physiological microenvironment.<sup>32</sup> Overall, the surface presentation of methacryloyl groups on the nanofiber enables facile incorporation of other desired photo-curable monomers or biopolymers, allowing for a flexible design and customization of copolymers or hybrids for specific application needs.

### 3.3 Quantitative analysis of the fragmented microgel and the porosity of the granular hydrogel

Fig. 2 illustrates the fluorescence staining images of the microgels sieving from photocured bulk hydrogels with 150/60  $\mu\text{m}$  mesh, along with the changes in Feret diameter and aspect ratio. Feret diameter is commonly used to measure the size of irregular particles and is defined as the distance between two parallel tangential lines on the 2D projection of a 3D objective.



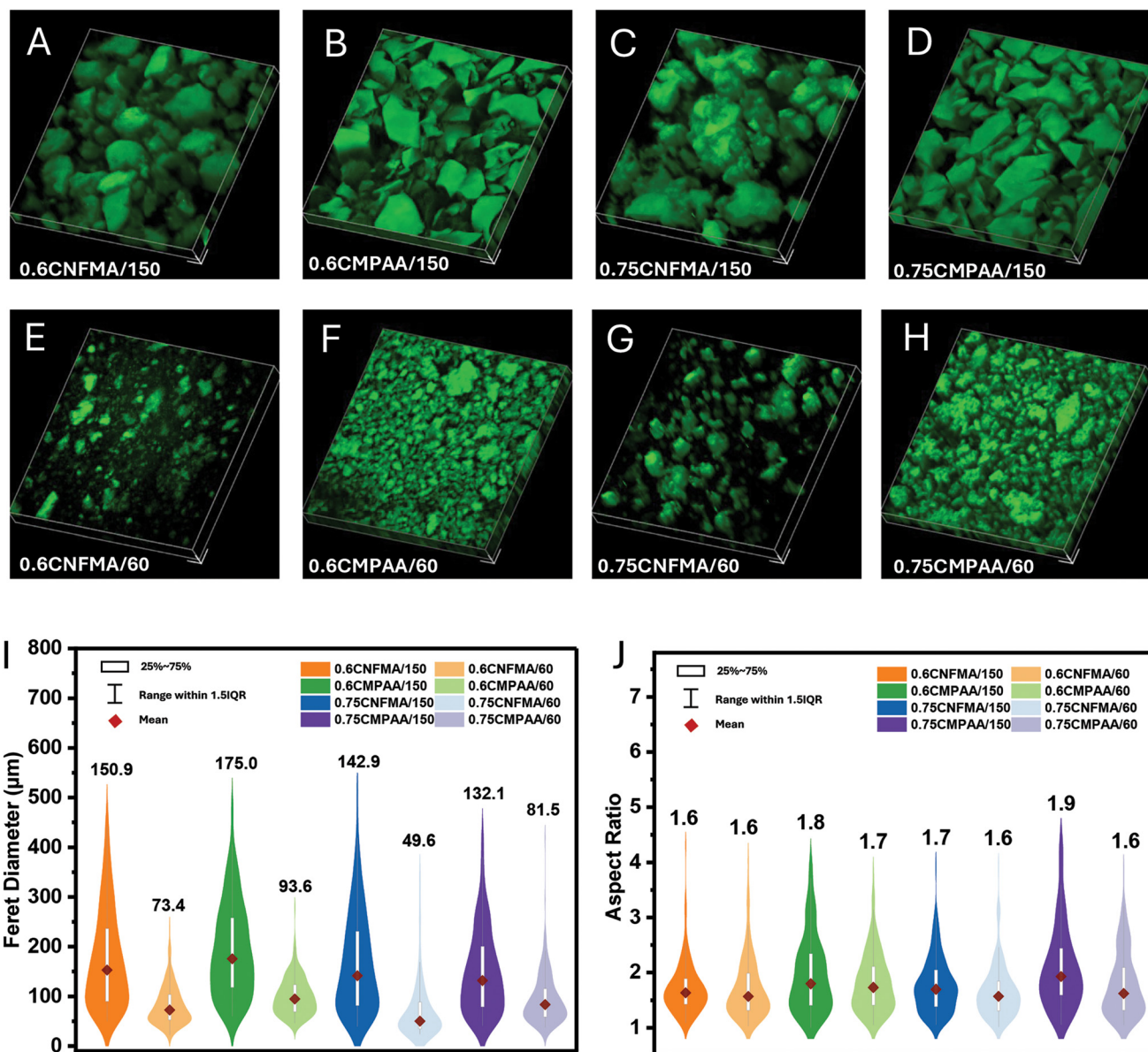


Fig. 2 Microgel visualization and quantitative analysis. (A–H) 3D reconstructed confocal microscopy images of fluorescently labeled CNFMA-based microgels obtained by passing through a 150/60 μm mesh (scale bars: 100 μm). (I) Feret diameter distribution and (J) aspect ratio measurements derived from Stacks analysis.

It provides insights into microgel size distribution and structure integrity, while the aspect ratio elucidates geometric deformation and anisotropic response of microgel under applied dynamic mechanical stress. After passing the samples through the 150 μm mesh, all samples exhibited relatively large Feret diameters (132.0–175.0 μm), with particle morphology remaining intact. Notably, the CMPAA samples displayed well-defined edges instead of a fluffy appearance of CNFMA, and their particle sizes were significantly larger than those of CNFMA samples at corresponding concentrations. This indicates that the introduction of PAA enhanced the structural stability of the particles, rendering the hydrogel system elastic at the bulk level, thus allowing it to dissipate stress more effectively under high

shear forces. In addition, the aspect ratio of CMPAA samples (1.8–1.9) was higher than that of CNFMA samples (1.6–1.7), suggesting that the localized rigidity of the CMPAA network plays a crucial role in maintaining a more regular particle shape under shear. The rigidity helps preserve particle integrity, while the bulk softness facilitates stress dissipation across the system, preventing excessive fragmentation or deformation under shear forces. Samples processed through the 60 μm mesh exhibited pronounced particle fragmentation and a significant reduction in size, with Feret diameters ranging from 49.6 to 93.6 μm. Notably, the high-concentration 0.75CNFMA sample displayed the smallest Feret diameter of 49.6 μm, highlighting the mechanical fragility of the pure cellulose fiber network under



shear forces. This fragility can be attributed to localized weak zones within the network, which disrupt stress transmission and prevent effective stress dissipation. Additionally, the high concentration of cellulose may hinder network rearrangement under pressure, further reducing the mobility of individual fibers and exacerbating the network's susceptibility to failure under shear. In contrast, CMPAA samples demonstrated less size reduction and a more uniform size distribution, as indicated by narrower violin plots. For example, the Feret diameter of the 0.75CMPAA sample (81.5  $\mu\text{m}$ ) was significantly larger than that of the 0.75CNFMA sample (49.6  $\mu\text{m}$ ). This observation underscores the critical role of PAA in reinforcing the structural stability of the hydrogel particles, thereby enhancing their resistance to shear forces. The aspect ratios of all samples passed through 60  $\mu\text{m}$  mesh within 1.6–1.7, indicating a tendency toward isotropic particle morphology under high shear forces. These results highlight the dual mechanical advantages introduced by the incorporation of PAA, improving the structural stability and resistance of the hydrogel particles to shear-induced fragmentation, while maintaining more regular and stable particle morphologies under dynamic mechanical stress.

A high macroporosity of granular hydrogels is a desirable property to support nutrient transport and cellular infiltration. To maintain a balance between mechanical stability and cellular compatibility, the pore diameter should ideally reach the microscale rather than the nanoscale.<sup>53</sup> The formation of porosity is closely linked to the size, morphology, and stacking behavior of the microgels. Granular hydrogels that were packed from microgels processed through the 150  $\mu\text{m}$  mesh exhibited higher porosity (19.0–30.9%) and more apparent pore structures compared with those processed through the 60  $\mu\text{m}$  mesh (Fig. 3A–H). CMPAA samples demonstrated the highest porosity under these conditions, which can be attributed to the balance between their rigidity and cohesion. The reduced deformability of CMPAA microgels created more void spaces, resulting in an interconnected porous structure with pore diameters reaching up to 100  $\mu\text{m}$  (Fig. 2J). In contrast, processing through the 60  $\mu\text{m}$  mesh resulted in significant microgel fragmentation, leading to smaller Feret diameters and denser packing, which dramatically reduced the porosity in both systems. The lowest porosity observed was in 0.6CMPAA/60 (6.2%), with a pore size around 15  $\mu\text{m}$  (Fig. 3H). The smaller and more fragmented microgel morphology in CNFMA provides a greater surface area and exposes more  $\text{COO}^-$  groups, facilitating more crosslinking points for  $\text{Ca}^{2+}$  and further reducing void spaces. However, this denser granular hydrogel assembled from the microgel passing through 60  $\mu\text{m}$  limited the cell viability in long-term 3D culture, as shown in Fig. S2.† Therefore, only granular hydrogels obtained from the microgel passing through 150  $\mu\text{m}$  were used for further 3D culture evaluation of E1 and PANC-1 cell lines.

### 3.4 3D culture evaluation for E1 and PANC-1 cell lines

Granular hydrogels are constructed by processing microgels through a 150  $\mu\text{m}$  mesh, followed by dilution and random

packing. Subsequent crosslinking with  $\text{Ca}^{2+}$  ions enables the formation of scaffolds characterized by tunable porosity (>19%) and stiffness (2–5 kPa), rendering them a suitable platform for 3D cell culture applications. E1 and PANC-1 cell lines are frequently employed to assess the performance of granular hydrogels, as they exhibit distinct morphological differences between 2D and well-optimized 3D culture conditions.<sup>2,7</sup>

As presented in Fig. 4C, the metabolic activity of E1 cells cultured on CNFMA and CMPAA hydrogel systems exhibited a consistent and significant proliferation trend over 14 days. Notably, the 0.75CMPAA granular hydrogel demonstrated the highest proliferation rate, whereas the 0.6CNFMA sample displayed the lowest. Incorporating PAA into the hybrid hydrogel scaffolds substantially enhanced E1 cell proliferation compared with the corresponding concentrations of pure CNFMA samples.

Further evaluation through live/dead staining confirmed the viability of E1 cells cultured in 3D within the granular hydrogel scaffolds. All granular hydrogels supported high cell viability over the 14 day culture period, as indicated by the dominance and progressive intensification of green fluorescence signals. Moreover, cells were uniformly distributed throughout the hydrogel scaffolds (Fig. 4A). This can be attributed to the macroporous structure and the cytocompatibility of the hydrogel system. Additionally, using HEPES and mannitol buffers during the cell-seeding process effectively maintained osmotic pressure during cell-microgel mixing, while the presence of 100 mM calcium ions did not adversely affect cell viability. However, in the 0.6CNFMA sample with the lowest stiffness and porosity, E1 cells exhibited more spherical morphology within 7 days, in contrast to the pronounced spreading along the microgel surface observed in other samples. This indicates weaker cell–cell and cell–matrix interactions (Fig. 4A and Fig. S3†). Cytoskeletal staining further confirmed that the 0.6CNFMA sample exhibited the lowest nuclear density and the weakest F-actin signal, with F-actin localized predominantly at the cell edges rather than evenly distributed across the samples. The pronounced F-actin signal indicates that the reduced proliferation rate observed at day 14 compared with day 7 may be attributable to spatial limitations (Fig. 4B). Interestingly, although the 0.6CMPAA and 0.75CNFMA granular hydrogels exhibit comparable average Young's moduli, F-actin staining revealed notable differences in cytoskeletal organization between the two samples. In the 0.6CMPAA hydrogel, the F-actin network was dense, continuous, and highly interconnected, indicative of enhanced cytoskeletal tension, robust cell–matrix adhesion, and the promotion of three-dimensional expansion. The actin filaments were uniformly distributed, suggesting a microenvironment that facilitates cell–cell connections and cytoskeletal stability. Conversely, the 0.75CNFMA hydrogel displayed a sparse and discontinuous F-actin network with visible gaps and thinner fibers. Cells within this hydrogel exhibited a flattened morphology, diminished cytoskeletal tension, and weaker cell–matrix interactions. This uneven distribution of F-actin reflects a less supportive environment, thereby restricting 3D expansion.



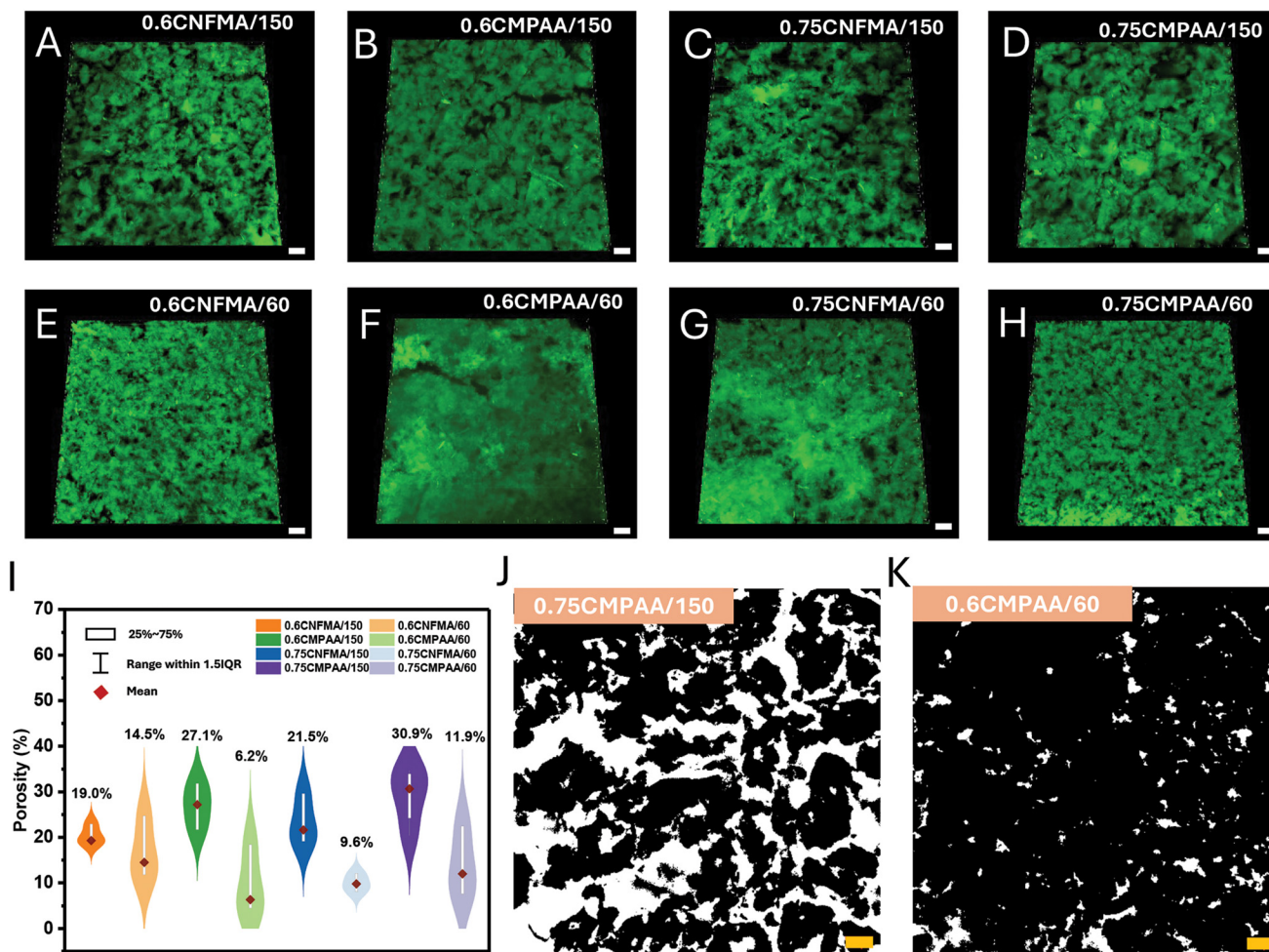


**Fig. 3** Visualization and quantitative analysis of granular hydrogels. (A–H) 3D reconstructions of volumetric stacks of fluorescently labeled CNFMA-based granular hydrogels (scale bars: 100  $\mu$ m). (I) Porosity of representative granular hydrogels calculated from image stacks using a custom macro in ImageJ. Threshold visualization of a single stack of (J) 0.75CMPAA and (K) 0.6CMPAA/60 granular hydrogels (scale bars: 100  $\mu$ m). Black areas represent stacked microgels, while white areas represent porous regions.

sion and compromising cytoskeletal organization. Biomechanical cues, such as stiffness, are critical extracellular signals regulating cellular responses. When cells adhere to hydrogels, integrins on the cell surface bind to adhesive ligands on the hydrogel surface, forming focal adhesion complexes that connect the ECM to the intracellular F-actin cytoskeleton. In other words, cells sense mechanical cues from the ECM through focal adhesion pathways, thereby modulating cytoskeletal tension.<sup>32,54,55</sup> The optimal stiffness facilitates fibroblast spreading and structural organization, promoting the formation of focal adhesions and actin stress fibers while resembling the mechanical properties of soft tissues. On softer substrates, they remain rounded with limited cytoskeletal organization.<sup>56,57</sup> This explains why E1 cells on the lowest-stiffness 0.6CNFMA sample (effective Young's modulus  $\approx$ 2 kPa) exhibited reduced cytoskeletal tension and limited spreading. On the other hand, premixed microgels incubated overnight with their respective culture medium allow a portion

of proteins to adsorb onto the microgel surface. This phenomenon is attributed to the  $\text{COO}^-$  group, which is recognized as an effective adsorbent for specific proteins.<sup>58</sup> Through electrostatic interactions, the negatively charged  $\text{COO}^-$  groups on CNFMA may bind to positively charged regions of proteins in the culture medium or cell membrane receptors, thereby enhancing cell attachment.

The incorporation of PAA enhances the hydrogel's mechanical properties by introducing localized stiffness heterogeneity within the CMPAA samples. This "patchy" stiffness distribution arises from the heterogeneous cross-linking density in this system, where regions with denser PAA chains exhibit higher stiffness, while areas with lower or no bridge of PAA show reduced mechanical properties. In contrast, the pure CNFMA network has a comparatively uniform structure with relatively consistent stiffness throughout. This uneven distribution endows CMPAA samples with more complex mechanical characteristics, as reflected in the effective Young's



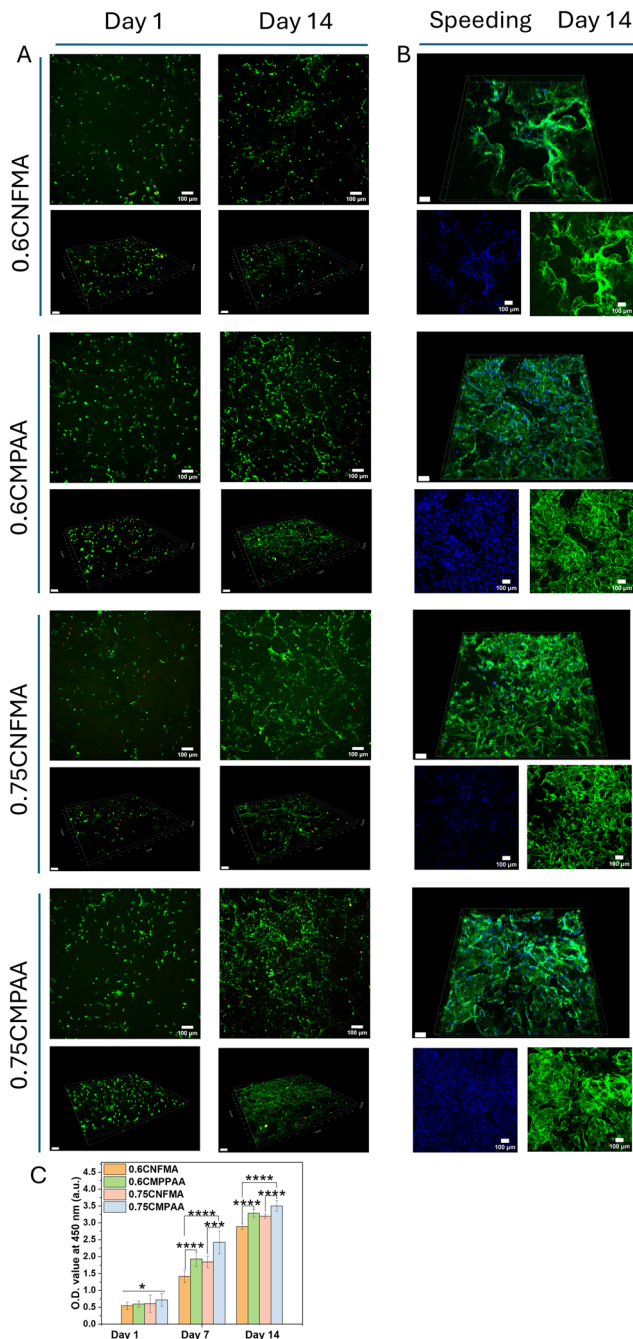


**Fig. 4** Evaluation of E1 cell viability, morphology, and proliferation within CNFMA-based granular hydrogels. (A) Representative fluorescence microscopy and 3D reconstruction images of live/dead staining in granular hydrogels on days 1 and 14 (live cells: green; dead cells: red), scale bar: 100  $\mu\text{m}$ . (B) 3D reconstruction and fluorescence microscopy images illustrating cytoskeletal organization in granular hydrogels on day 14 (F-actin: green; nuclei: blue). (C) Quantitative analysis of MC3T3-E1 cell viability within the granular hydrogels on day 1, 7, and 14. Statistical analysis: \* $p < 0.05$ , \*\* $p < 0.01$ , and \*\*\* $p < 0.001$ ,  $n = 3$ .

modulus data in Fig. 1J. The boxplot for CNFMA samples shows a much narrower stiffness distribution, indicating greater uniformity in mechanical properties. In contrast,

CMPAA samples exhibit a broader IQR (*i.e.*, 0.75CMPAA of 3.7–5.8 kPa IQR), underlining a heterogeneity in their local stiffness. Regions with higher stiffness generate stronger traction forces, prompting E1 cells to ‘explore’ and migrate toward these areas. This mechanotactic behavior leads to the formation of thicker and more concentrated F-actin fibers at mechanical hotspots, ultimately enhancing overall cytoskeletal tension in E1 cells.<sup>54,55</sup>

Incorporating PAA into the CNFMA matrix is key to generating this microscale mechanical heterogeneity. Although bulk PAA is considered biologically inert, its copolymerization with CNFMA appears to produce localized “patchy” domains with distinct mechanical and potentially cell-interactive surface charges from amine groups. In particular, while CNFMA surfaces are dominated by negatively charged carboxyl groups, the presence of amide or possibly protonated amine groups in PAA may introduce localized positive charges. Given the negatively charged nature of cell membranes, such subtle charge variations may further support cell attachment through electrostatic interactions. However, the influence of surface chemistry was not independently verified in this study. Thus, our interpretation focuses primarily on the mechanical aspects of the hybrid system.

Tumor cells in 3D culture environments have been shown to respond to environmental stimuli and signals significantly differ from traditional 2D cultures.<sup>2</sup> Traditional 3D tumor cell culture methods often use encapsulation techniques to observe cell aggregation behavior.<sup>59–61</sup> However, encapsulated cells are embedded within the 3D matrix, which restricts effective intercellular communication and impairs specific migration activities of tumor cells. Therefore, to achieve more accurate dynamic monitoring, tumor cells are better placed in a more “open” matrix environment that facilitates cell–cell interactions and migration behaviors. The dual cross-linking structure of CNFMA enables PANC-1 cells to distribute uniformly within the pores after being mixed with microgels, supporting significant proliferation during long-term culture for over 14 days (Fig. 5C). On Day 1, PANC-1 cells in the 0.75CMPAA sample which exhibited the highest Young’s modulus demonstrated lower initial activity compared with other samples. This reduced activity may result from the preferential accumulation of cells in stiffer regions, driven primarily by their efforts to explore and adapt to the surrounding environment rather than differences in proliferation. During the first 7 days of culture, distinct trends were observed: cell proliferation declined in the 0.6CNFMA and 0.75CNFMA samples, while the 0.6CMPAA and 0.75CMPAA samples, characterized by localized stiffness, showed a slight increase in proliferation. Taken together, these data suggest that the localized stiffness of CMPAA samples creates a microenvironment that promotes cell migration and supports moderate proliferation over time, aligning with findings from previous research.<sup>59–61</sup>

PANC-1 cells display different adaptive behaviors in response to the contrasting mechanical properties of CNFMA and CMPAA granular hydrogels. In low-stiffness CNFMA



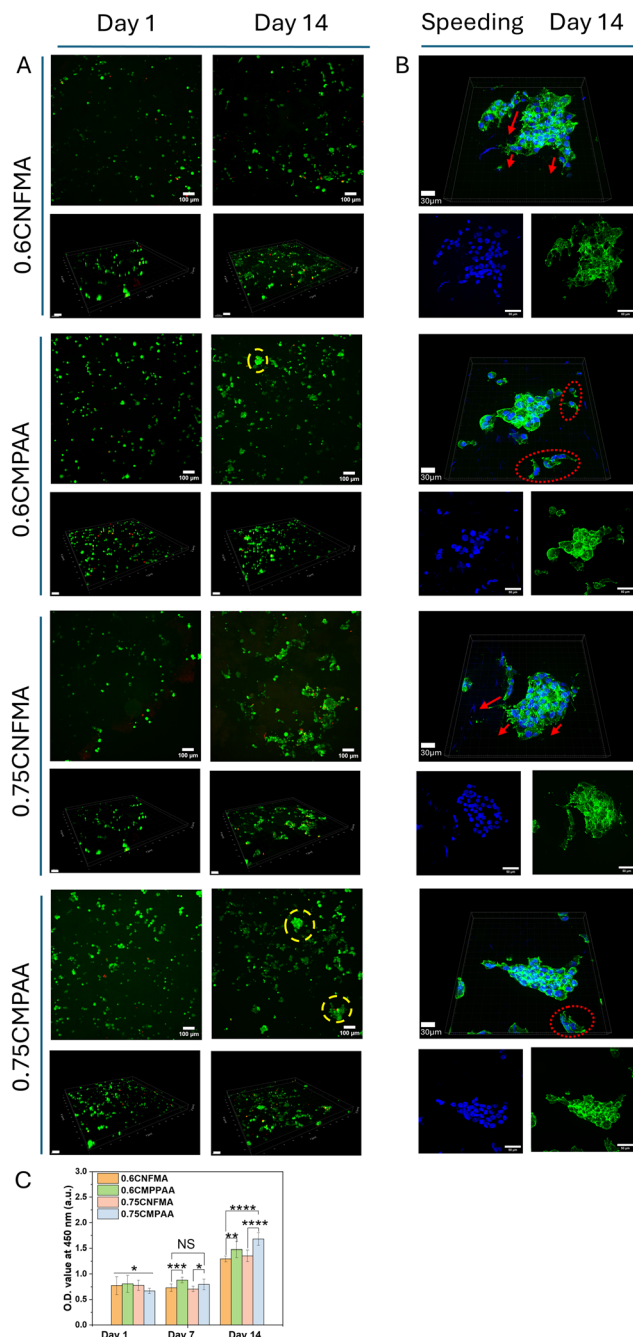


**Fig. 5** Evaluation of PANC-1 cell viability, morphology, and proliferation within CNFMA-based granular hydrogels. (A) Representative fluorescence microscopy and 3D reconstruction images of live/dead staining in granular hydrogels on days 1 and 14 (live cells: green; dead cells: red), scale bar: 100  $\mu\text{m}$ . (B) 3D reconstruction and fluorescence microscopy images illustrating cytoskeletal organization in granular hydrogels on day 14 (F-actin: green; nuclei: blue). (C) Quantitative analysis of MC3T3-E1 cell viability within the granular hydrogels on days 1, 7, and 14. Statistical analysis: \* $p < 0.05$ , \*\* $p < 0.01$ , \*\*\* $p < 0.001$ ,  $n = 3$ .

matrices, cytoskeletal staining revealed that cells exhibit loosely distributed, flattened structures (Fig. 5B and Fig. S4†). Elongated F-actin structures at the cell edges indicated active probing of the surrounding matrix *via* lamellipodia and filopo-

dia. Furthermore, the presence of synapse-like F-actin connections between distant cells suggests that PANC-1 cells utilize actin-based structures for communication and coordination of collective migration. These behaviors reflect the dynamic adaptability of PANC-1 cells, as the permissive environment provided by CNFMA supports moderate adhesion and mechanical signal transduction without promoting the formation of compact spheroids.

In contrast, CMPAA hydrogels with localized stiffness create a microenvironment that elicits a distinct cellular response. Live/dead (L/D) staining on day 14 revealed significant spherical aggregates of PANC-1 cells in CMPAA samples while cytoskeletal staining revealed that cells exhibited more tightly packed nuclei, with F-actin primarily concentrated at the periphery of the compact spheroids, forming a clear cortical F-actin structure (Fig. 5A, yellow cycle; Fig. 5B). During the early stages (7 days), PANC-1 cells responded positively to localized stiffness, demonstrating higher proliferation rates. However, matrix adhesion sites became saturated and cell-cell adhesion began to dominate as cell density increased. This shift drove the cells to transition from an extended morphology to compact 3D spheroids, minimizing energy expenditure while inhibiting their migration and spreading capabilities. These spheroid structures reduced shear forces and mechanical stress experienced by the cells, but excessive reliance on cell-cell adhesion may limit the dynamic adaptability of tumor cells, particularly during invasion. The lack of lamellipodia or filopodia extending toward the matrix suggests a reduced exploratory behavior under these conditions.

Mechanistically, the differences between the two hydrogels are closely tied to their structural features and the biochemical cues they provide. The uniformly distributed CNFMA matrix exposes abundant carboxyl groups, enhancing integrin-mediated signaling pathways and promoting cell-matrix adhesion. This supports lamellar structures, where cells remain dispersed, dynamically probing their surroundings, and exhibiting collective migration. In contrast, localized stiffness in CMPAA hydrogels promotes spheroid formation, characterized by strong cell-cell adhesion that reduces shear forces and mechanical stress but inhibits invasive behaviors. Polarized morphologies observed in individual cells or small protrusive cell clusters within 0.6/0.75CMPAA samples, with protrusions resembling lamellipodia or filopodia, further indicate migratory tendencies (Fig. 5B, red circle), although this behavior diminishes as spheroids mature.

These findings highlight the adaptability of PANC-1 cells to their microenvironment, with CNFMA and CMPAA hydrogels offering complementary platforms for studying tumor biology. The lamellar structures formed in CNFMA samples are ideal for investigating tumor edge behavior, migration, and invasion, while the compact spheroids in CMPAA samples provide insights into the metabolic properties, nutrient absorption, and stem cell-like characteristics of tumor cores. By constructing interconnected porous networks, these hydrogels comprehensively simulate the diverse microenvironments encountered by PANC-1 tumors.



## 4. Conclusion

In this work, we developed granular hydrogel platforms derived from photocurable CNFMAs and their copolymers with PAA. By simply sieving the photocured bulk hydrogel into microgels and then ionically crosslinking these microgels together with cells, we achieved an open and porous network with tunable local stiffness and enhanced cell–matrix interactions. Comparative studies using MC3T3-E1 and PANC-1 cells showed that the uniformly distributed, low-stiffness CNFMA promoted integrin-mediated adhesion and lamellar morphologies in PANC-1. In contrast, the “patchy” stiffness distribution in CMPAA triggered localized cytoskeletal tension in MC3T3-E1 and led to compact spheroid formation in PANC-1. These distinct growth responses underscore the versatility of our granular hydrogels in supporting a wide range of cellular behaviors in long-term 3D culture, spanning from robust osteoblastic proliferation to tumor-like, spheroid-driven phenotypes. Overall, this photocurable CNF-based hydrogel platforms overcome the limitations of pristine nanocellulose hydrogels by offering customizable biomechanical cues, straightforward preparation and robust cell viability, thus making them promising tools for advancing 3D cell culture in both tissue engineering and tumor biology.

## Author contributions

Conceptualization and methodology: S. Liang, Q. Wang, and X. Wang; formal analysis: S. Liang; data curation: S. Liang; investigation: S. Liang, Q. Wang, and X. Wang; visualization and validation: S. Liang; supervision: C. Xu, J.M. Rosenholm, and X. Wang; resources, funding acquisition and project administration: C. Xu, J.M. Rosenholm, and X. Wang; writing – original – draft: S. Liang; writing – review & editing: S. Liang, Q. Wang, C. Xu, J.M. Rosenholm, and X. Wang.

## Data availability

This research paper is accompanied by one ESI.† The dataset supporting this study is openly available in a public repository at <https://etsin.fairdata.fi>. Accessible through the following link: <https://etsin.fairdata.fi/dataset/09839129-c92b-483b-857c-58d35a784635>.

## Conflicts of interest

There are no conflicts of interest to declare.

## Acknowledgements

Business Finland is acknowledged for funding this study via the Research-to-Business project 3D CelluGel (1529/31/2022). S. Liang would like to acknowledge the financial

support from the Doctoral Network of Åbo Akademi University (ÅAU) for funding her doctoral study at ÅAU, Finland. X. Wang would like to thank the Research Council of Finland for the Academy Research Fellow funding (333158) at ÅAU. This research is also aligned with the strategic research profiling area “Solutions for Health” at Åbo Akademi University (funded by the Research Council/Academy of Finland, 336355). Parts of the research used the Research Council of Finland Research Infrastructure “Printed Intelligence Infrastructure” (PII-FIRI).

## References

- 1 K. A. Fitzgerald, M. Malhotra, C. M. Curtin, F. J. O'Brien and C. M. O'Driscoll, *J. Controlled Release*, 2015, **215**, 39–54.
- 2 O. Habanjar, M. Diab-Assaf, F. Caldefie-Chezet and L. Delort, *Int. J. Mol. Sci.*, 2021, **22**, 12200.
- 3 N. Chaicharoenaudomrung, P. Kunhorm and P. Noisa, *World J. Stem Cells*, 2019, **11**, 1065.
- 4 C. Jensen and Y. Teng, *Front Mol. Biosci.*, 2020, **7**, 513823.
- 5 M. Ravi, V. Paramesh, S. R. Kaviya, E. Anuradha and F. D. Paul Solomon, *J. Cell. Physiol.*, 2015, **230**, 16–26.
- 6 M. A. G. Barbosa, C. P. R. Xavier, R. F. Pereira, V. Petrikaitė and M. H. Vasconcelos, *Cancers (Basel)*, 2022, **14**, 190.
- 7 T. Zhang, S. Lin, X. Shao, Q. Zhang, C. Xue, S. Zhang, Y. Lin, B. Zhu and X. Cai, *Cell Proliferation*, 2017, **50**, 50.
- 8 M. P. Nikolova and M. S. Chavali, *Bioact. Mater.*, 2019, **4**, 271–292.
- 9 S. Naahidi, M. Jafari, M. Logan, Y. Wang, Y. Yuan, H. Bae, B. Dixon and P. Chen, *Biotechnol. Adv.*, 2017, **35**, 530–544.
- 10 T. Falcucci, M. Radke, J. K. Sahoo, O. Hasturk and D. L. Kaplan, *Biomaterials*, 2023, **300**, 122201.
- 11 C. D. Spicer, *Polym. Chem.*, 2020, **11**, 184–219.
- 12 Z. Wang, Q. Ye, S. Yu and B. Akhavan, *Adv. Healthcare Mater.*, 2023, **12**, 2300105.
- 13 G. Sennakesavan, M. Mostakhdemin, L. K. Dkhar, A. Seyfoddin and S. J. Fatihhi, *Polym. Degrad. Stab.*, 2020, **180**, 109308.
- 14 A. Z. Unal and J. L. West, *Bioconjugate Chem.*, 2020, **31**, 2253–2271.
- 15 A. C. Duarte, E. C. Costa, H. A. L. Filipe, S. M. Saraiva, T. Jacinto, S. P. Miguel, M. P. Ribeiro and P. Coutinho, *Biomater. Adv.*, 2023, **151**, 213428.
- 16 A. Gebeyehu, S. K. Surapaneni, J. Huang, A. Mondal, V. Z. Wang, N. F. Haruna, A. Bagde, P. Arthur, S. Kutlehria, N. Patel, A. K. Rishi and M. Singh, *Sci. Rep.*, 2021, **11**, 372.
- 17 M. D. Cherne, B. Sidar, T. A. Sebrell, H. S. Sanchez, K. Heaton, F. J. Kassama, M. M. Roe, A. B. Gentry, C. B. Chang, S. T. Walk, M. Jutila, J. N. Wilking and D. Bimczok, *Front. Pharmacol.*, 2021, **12**, 707891.
- 18 X. Wang, Q. Wang and C. Xu, *Bioengineering*, 2020, **7**, 40.
- 19 A. Subhedar, S. Bhadauria, S. Ahankari and H. Kargarzadeh, *Int. J. Biol. Macromol.*, 2021, **166**, 587–600.
- 20 L. Lin, S. Jiang, J. Yang, J. Qiu, X. Jiao, X. Yue, X. Ke, G. Yang and L. Zhang, *Int. J. Bioprint.*, 2022, **9**, 637.
- 21 F. Rol, M. N. Belgacem, A. Gandini and J. Bras, *Prog. Polym. Sci.*, 2019, **88**, 241–264.



- 22 M. Y. Khalid, Z. U. Arif, A. Al Rashid, S. M. Z. S. Bukhari, M. Hossain and M. Koç, *Giant*, 2024, 100299.
- 23 N. S. Sharip and H. Ariffin, *Mater. Today Proc.*, 2019, **16**, 1959–1968.
- 24 J. Alkabli, W. N. El-Sayed, R. F. M. Elshaarawy and A. I. M. Khedr, *Eur. Polym. J.*, 2020, **138**, 109960.
- 25 Q. Wang, Ö. Karadas, J. M. Rosenholm, C. Xu, T. Näreojä and X. Wang, *Adv. Funct. Mater.*, 2024, **34**, 2400431.
- 26 I. Nikolits, S. Radwan, F. Liebner, W. Dietrich, D. Egger, F. Chariyev-Prinz and C. Kasper, *ACS Appl. Bio Mater.*, 2023, **6**, 543–551.
- 27 J. G. Torres-Rendon, M. Köpf, D. Gehlen, A. Blaeser, H. Fischer, L. De Laporte and A. Walther, *Biomacromolecules*, 2016, **17**, 905–913.
- 28 J. Rosendahl, A. Svanström, M. Berglin, S. Petronis, Y. Bogestål, P. Stenlund, S. Standoft, A. Ståhlberg, G. Landberg, G. Chinga-Carrasco and J. Håkansson, *Bioengineering*, 2021, **8**, 97.
- 29 P. Balaji, A. Murugadas, L. Paasonen, S. Shanmugaapriya, M. A. Akbarsha, P. Balaji, A. Murugadas, L. Paasonen, S. Shanmugaapriya and M. A. Akbarsha, *AIMS Biophys.*, 2022, **9**, 221–234.
- 30 V. Zaderer, M. Hermann, C. Lass-Flörl, W. Posch and D. Wilflingseder, *Cells*, 2019, **8**, 1292.
- 31 J. Li, Y. Liu, Y. Zhang, B. Yao, B. Enhejirigala, Z. Li, W. Song, Y. Wang, X. Duan, X. Yuan, X. Fu and S. Huang, *Front. Cell Dev. Biol.*, 2021, **9**, 640388.
- 32 X. Dong, Q. Sun, J. Geng, X. Liu and Q. Wei, *Nano Lett.*, 2024, **24**, 4029–4037.
- 33 Q. Wei, S. Wang, F. Han, H. Wang, W. Zhang, Q. Yu, C. Liu, L. Ding, J. Wang, L. Yu, C. Zhu and B. Li, *Biomaterials Transl.*, 2021, **2**, 323.
- 34 V. Guccini, J. Phiri, J. Trifol, V. Rissanen, S. M. Mousavi, J. Vapaavuori, T. Tammelin, T. Maloney and E. Kontturi, *ACS Appl. Polym. Mater.*, 2022, **4**, 24–28.
- 35 S. Sinquefield, P. N. Ciesielski, K. Li, D. J. Gardner and S. Ozcan, *ACS Sustainable Chem. Eng.*, 2020, **8**, 9601–9615.
- 36 J. R. McKee, E. A. Appel, J. Seitsonen, E. Kontturi, O. A. Scherman and O. Ikkala, *Adv. Funct. Mater.*, 2014, **24**, 2706–2713.
- 37 H. D. Nguyen, H. Y. Liu, B. N. Hudson and C. C. Lin, *ACS Biomater. Sci. Eng.*, 2019, **53**, 1247–1256.
- 38 A. Fiorati, C. Linciano, C. Galante, M. G. Raucci and L. Altomare, *Materials*, 2021, **14**, 4511.
- 39 Q. Feng, D. Li, Q. Li, X. Cao and H. Dong, *Bioact. Mater.*, 2022, **9**, 105–119.
- 40 A. C. Daly, L. Riley, T. Segura and J. A. Burdick, *Nat. Rev. Mater.*, 2020, **5**, 20–43.
- 41 A. C. Daly, *Adv. Healthcare Mater.*, 2024, **13**, 2301388.
- 42 D. B. Gehlen, N. Jürgens, A. Omidinia-Anarkoli, T. Haraszti, J. George, A. Walther, H. Ye and L. De Laporte, *Macromol. Rapid Commun.*, 2020, **41**, 2000191.
- 43 Y. Brusentsev, P. Yang, A. W. T. King, F. Cheng, M. F. Cortes Ruiz, J. E. Eriksson, I. Kilpeläinen, S. Willför, C. Xu, L. Wågberg and X. Wang, *Biomacromolecules*, 2023, **24**, 3835–3845.
- 44 A. Isogai, T. Saito and H. Fukuzumi, *Nanoscale*, 2011, **31**, 71–85.
- 45 J. Liao, K. A. Pham and V. Breedveld, *Cellulose*, 2021, **28**, 813–827.
- 46 S. Metwally, S. Ferraris, S. Spriano, Z. J. Krysiak, Ł. Kaniuk, M. M. Marzec, S. K. Kim, P. K. Szewczyk, A. Gruszczyński, M. Wytrwal-Sarna, J. E. Karbowniczek, A. Bernasik, S. Kar-Narayan and U. Stachewicz, *Mater. Des.*, 2020, **194**, 108915.
- 47 J. Liu, F. Cheng, H. Grénman, S. Spoljaric, J. Seppälä, J. E. Eriksson, S. Willför and C. Xu, *Carbohydr. Polym.*, 2016, **148**, 259–271.
- 48 R. V. Barrulas and M. C. Corvo, *Gels*, 2023, **9**, 986.
- 49 J. Karvinen, T. O. Ihalainen, M. T. Calejo, I. Jönkkäri and M. Kellomäki, *Mater. Sci. Eng. C Mater. Biol. Appl.*, 2019, **94**, 1056–1066.
- 50 Q. Wang, O. Backman, M. Nuopponen, C. Xu and X. Wang, *Front. Chem. Eng.*, 2021, **3**, 723429.
- 51 A. Corker, H. C. H. Ng, R. J. Poole and E. García-Tuñón, *Soft Matter*, 2019, **15**, 1444–1456.
- 52 M. Zambito, F. Viti, A. G. Bosio, I. Ceccherini, T. Florio and M. Vassalli, *Nanomaterials*, 2023, **13**, 1190.
- 53 L. Shao, Q. Gao, C. Xie, J. Fu, M. Xiang, Z. Liu, L. Xiang and Y. He, *Biodes. Manuf.*, 2020, **3**, 30–39.
- 54 P. Kanchanawong and D. A. Calderwood, *Nat. Rev. Mol. Cell Biol.*, 2022, **24**, 142–161.
- 55 D. S. Gray, J. Tien and C. S. Chen, *J. Biomed. Mater. Res., Part A*, 2003, **66A**, 605–614.
- 56 T. Yeung, P. C. Georges, L. A. Flanagan, B. Marg, M. Ortiz, M. Funaki, N. Zahir, W. Ming, V. Weaver and P. A. Janmey, *Cell Motil. Cytoskeleton*, 2005, **60**, 24–34.
- 57 P. A. Janmey, J. P. Winer, M. E. Murray and Q. Wen, *Cell Motil. Cytoskeleton*, 2009, **66**, 597–605.
- 58 A. M. Rahmatika, Y. Goi, T. Kitamura, W. Widiyastuti and T. Ogi, *Mater. Sci. Eng. C*, 2019, **105**, 110033.
- 59 H. Y. Liu, M. Korc and C. C. Lin, *Biomaterials*, 2018, **160**, 24–36.
- 60 H. Y. Liu, T. Greene, T. Y. Lin, C. S. Dawes, M. Korc and C. C. Lin, *Acta Biomater.*, 2017, **48**, 258–269.
- 61 C. S. Ki, H. Shih and C. C. Lin, *Biomacromolecules*, 2013, **14**, 3017–3026.

